Visual reconstruction of flexible structure based on fiber grating sensor array and extreme learning machine algorithm*

ZHANG Sisi[1], YAN Jie[1], JIANG Mingshun[1], SUI Qingmei[1], ZHANG Lei[1], and LUO Yuxiang[2]**

1. School of Control Science and Engineering, Shandong University, Jinan 250061, China

2. Shandong Institute of Space Electronic Technology, Jinan 250061, China

(Received 13 December 2021; Revised 8 March 2022)

©Tianjin University of Technology 2022

A visual reconstruction method was proposed based on fiber Bragg grating (FBG) sensors and an intelligent algorithm, aiming to solve the problems of low accuracy and complex reconstruction process in conventional reconstruction methods of flexible structures. Firstly, the wavelength data containing structural strain information was captured by FBG sensors, together with deformation displacement information. Subsequently, a predicted model was built based on an extreme learning machine (ELM) and further optimized by the particle swarm optimization (PSO) algorithm. Different deformation patterns were tested on an aluminum alloy plate, indicating the ability of the predicted model to produce the deformation displacement for reconstruction. The experimental results show that the maximum error can be as low as 0.050 mm, which verifies that the proposed method is feasible and satisfied with the deformation monitoring of the spacecraft structure.

Document code: A **Article ID:** 1673-1905(2022)07-0390-8

DOI https://doi.org/10.1007/s11801-022-1189-4

The flexible structures especially aluminum alloy plates have a wide array of applications in the aerospace field. Monitoring the deformation state of these typical structures, due to the complex flight environment and operating conditions, plays an important role in ensuring the safety and working performance of spacecraft.

Measuring the strain is the basis for realizing the reconstruction of deformed structures. Compared with some traditional strain measurement methods, including strain gauge electrical measurement method, photo elastic method, laser scanning measurement method[1-3], the fiber Bragg grating (FBG) sensor has unique advantages, such as strong anti-interference ability, high measurement accuracy, and distributed survey. The sensor has great potential for research and health monitoring in the spacecraft structures operating in the high-speed and complex flight environment[4-6]. Therefore, we will use FBG sensors to perform strain measurements of the aluminum alloy plate structures.

There have been studies showing that the center wavelength shift of the FBG sensor corresponds well with the load subjected to the tested structures under the dynamic and static load[7], so to use FBG sensor is quite reasonable to obtain load information and enable surface reconstruction combining its advantages mentioned above. Considerable work has been conducted by several researchers in the field of three-dimensional surface reconstruction based on FBG sensors. One of the more commonly used methods is the curvature conversion method, whose basic principle is to convert the structural strain information into curvature information and then obtain the coordinate values of curvature points through numerical integration, supporting the surface reconstruction. ZHU et al[8,9] utilized this method to realize the reconstruction of the flexible curved surface and the dynamic visual display of a solar panel. WANG et al[10] designed an FBG sensor network to measure the spatial position of the conversion node based on the segmental constant curvature-deflection assumption and realized the visual reconstruction of the three-dimensional shape of the soft manipulator. ZHENG et al[11] also established a geometric model of the unit surface reconstruction of the solar panel successfully by the way of recursion based on the curvature conversion method. However, it inevitably needs a large number of complex arithmetic processes, causing to accumulate errors in calculation.

* This work has been supported by the National Natural Science Foundation of China (Nos.62073193, 61903224, 61873333 and 61903225), the National Key Research and Development Project (Nos.2018YFE02013 and 2020YFE0204900), the Key Research and Development Plan of Shandong Province (Nos.2019TSLH0301 and 2019GHZ004), and the Natural Science Foundation of Shandong Province, China (No.ZR2021MF041).

** E-mail: drleizhang@sdu.edu.cn

The modal method indicates that the structural displacements can be estimated as the multiplication of the structural strains and adequate displacement-strain transformation (DST) matrix. THOMAS et al[12] applied the modal method to the strain-displacement model of the cantilever plate structure and achieved the deformation estimation of the static and dynamic deformation of the cantilever plate structure. BANG et al[13] realized the shape estimation of a wind turbine tower in a similar way. But to build a DST matrix is not easy, for material information such as load or elastic modulus required is too strict to be measured precisely during the experiment, which makes it difficult to reconstruct the modal matrix. On the other hand, TESSLER et al[14] put forward an inverse finite element method, introducing the principle of variation for the three-dimensional reconstruction of the plate structure by using discrete strain, which is not suitable for complex engineering structures. In conclusion, these methods mentioned above still have some of their defects that cannot be neglected.

Compared with these traditional methodologies, the neural network algorithm has received much attention[15,16], for it has the merit of no strict requirements on the simulation model and the powerful nonlinear modeling capability, so it has a good application prospect in the surface reconstruction of flexible structures. To date, one of the popular algorithms is the extreme learning machine (ELM), which is a kind of single hidden layer feedforward neural network, using an input weight matrix and a threshold weight matrix which are randomly generated to determine the output weight matrix at one time, and produces better generalization performance and faster training speed than the traditional back-propagation (BP) neural network[17-19]. WAN et al[20] developed a novel hybrid intelligent algorithm approach based on ELM for interval forecasting of wind power without the prior knowledge of forecasting errors successfully. An intelligent fault diagnosis method combined local mean decomposition-singular value decomposition with ELM was proposed by YE et al[21], which had the result of lessening human intervention and shortening the fault-diagnosis time. However, the input weight matrix and threshold matrix of the ELM are generated randomly, which will cause a certain size of prediction error. In order to further enhance its accuracy, in this paper, the particle swarm optimization (PSO) algorithm is chosen to adjust the parameters that are generated randomly of ELM to obtain the optimal ELM predicted model to reduce the prediction error with its strong global optimization capability[22-24].

This paper proposes a visual reconstruction method of the structure shape based on the FBG sensor array and the ELM optimized by the PSO algorithm, where the ELM is used to establish the complex relationship between strain and deformation displacement. For the proposed method can realize the direct conversion from strain to deformation, the steps are simplified and the accuracy of the surface reconstruction is improved compared with the traditional methods.

When a broadband light source within a fiber impinges on the fiber grating, only the specific light that meets the Bragg condition can be reflected, and the rest of the light is transmitted[25,26]. The Bragg equation is given as

$$\lambda_{\mathrm{B}} = 2n_{\mathrm{eff}}\Lambda, \quad (1)$$

where λ_{B} is the center wavelength of the FBG reflection spectrum, also known as the Bragg wavelength, which is governed by the effective refractive index n_{eff} and the grating period Λ.

The change of the temperature or stress of the environment in which the fiber grating is located results in a shift of the Bragg wavelength. When the temperature is controlled to remain unchanged during the experiment and the sensor is only subjected to strain, the relationship between the wavelength shift and the strain could be written as

$$\frac{\Delta\lambda_{\mathrm{B}}}{\lambda_{\mathrm{B}}} = \left(1 - P_{\mathrm{e}}\right)\varepsilon, \quad (2)$$

where $\Delta\lambda_{\mathrm{B}}$ expresses the Bragg wavelength offset, P_{e} is the elastic modulus of the fiber grating, and ε is the axis strain value. By measuring the shift of the reflected wavelength before and after the change, the change of strain can be obtained[27,28].

It can be seen from Eq.(2) that the Bragg wavelength offset has a linear relationship with the amount of strain. In other words, the change in the Bragg wavelength of the sensor caused by the deformation of the structure can reflect the strain of the structure, as well as the deformed displacement of the structure. Therefore, the wavelength information and deformation displacement information collected could be substituted into the ELM neural network optimized by the PSO algorithm for training to obtain a predicted model, and then the unknown displacement data could be predicted by the model according to the known wavelength. The ELM predicted model obtained before can be used to complete the surface reconstruction.

An ELM neural network in this paper consists of input layer, hidden layer, and output layer, as shown in Fig.1.

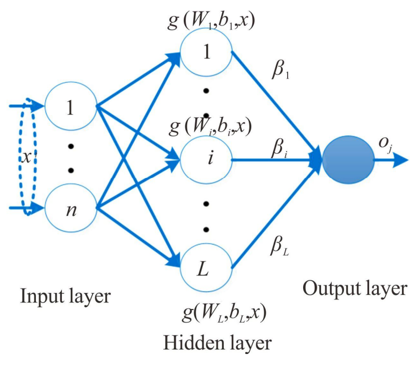

Fig.1 Structure of ELM

Supposing that there are N arbitrary samples ($\boldsymbol{X}_i$, $\boldsymbol{t}_i$), (i=1, 2,…,N), where $\boldsymbol{X}_i=[x_{i1}, x_{i2},\ldots,x_{in}]\in R^n$ denotes the input and $\boldsymbol{t}_i=[t_{i1}, t_{i2},\ldots,t_{im}]\in R^m$ denotes the actual output of the ELM model, set the number of hidden nodes to L, and then the mathematical expression of the ELM model can be described as

$$\sum_{i=1}^{L}\beta_i g\left(\boldsymbol{W}_i\cdot\boldsymbol{X}_j+\boldsymbol{b}_i\right)=\boldsymbol{o}_j,\left(j=1,2,\cdots,N\right), \tag{3}$$

where β_i refers to the output weight of the output layer, $\boldsymbol{W}_i=[W_{i1}, W_{i2},\ldots, W_{in}]^{\mathrm{T}}$ refers to the input weight of the input layer, $\boldsymbol{b}_i$ is the threshold of the ith hidden node, and $\boldsymbol{o}_i$ is the predicted output. $g(x)$ is defined as the activation function to increase the nonlinearity of the neural network, which is often used as

$$g\left(x\right)=\frac{1}{1+\mathrm{e}^{-x}}. \tag{4}$$

The purpose of this single hidden layer learning network is to approach the predicted output to the actual output as closely as possible, namely,

$$\sum_{j=1}^{n}\left\|\boldsymbol{o}_j-\boldsymbol{t}_j\right\|=0. \tag{5}$$

Combining Eq.(5) with Eq.(3), we expect to realize the best possible result that

$$\sum_{i=1}^{L}\beta_i g\left(\boldsymbol{W}_i\cdot\boldsymbol{X}_j+\boldsymbol{b}_i\right)=\boldsymbol{t}_j,\left(j=1,2,\cdots,N\right). \tag{6}$$

The math operation can be written compactly as $\boldsymbol{H\beta}=\boldsymbol{T}$, where $\boldsymbol{\beta}_{T\times m}$ represents the output weight matrix and the expected output matrix can be written as $\boldsymbol{T}_{N\times m}$. The output matrix of the hidden layer $\boldsymbol{H}$ can be expressed as

$$\boldsymbol{H}\left(\boldsymbol{W}_1,\cdots,\boldsymbol{W}_L,\boldsymbol{b}_1,\cdots,\boldsymbol{b}_L,\boldsymbol{X}_1,\cdots,\boldsymbol{X}_N\right)=$$
$$\begin{vmatrix} g\left(\boldsymbol{W}_1\cdot\boldsymbol{X}_1+\boldsymbol{b}_1\right) & \cdots & g\left(\boldsymbol{W}_L\cdot\boldsymbol{X}_1+\boldsymbol{b}_L\right)\\ \vdots & \cdots & \vdots\\ g\left(\boldsymbol{W}_1\cdot\boldsymbol{X}_N+\boldsymbol{b}_1\right) & \cdots & g\left(\boldsymbol{W}_L\cdot\boldsymbol{X}_N+\boldsymbol{b}_L\right)\end{vmatrix}_{N\times L}. \tag{7}$$

Thus, the training goal of ELM is to find the specific $\hat{\boldsymbol{W}}_i$, $\hat{\boldsymbol{b}}_i$ and $\hat{\boldsymbol{\beta}}_i$ to achieve Eq.(5), such that

$$\left\|\boldsymbol{H}\left(\hat{\boldsymbol{W}}_i,\hat{\boldsymbol{b}}_i\right)\hat{\beta}_i-\boldsymbol{T}\right\|=\min_{W,b,\beta}\left\|\boldsymbol{H}\left(\boldsymbol{W}_i,\boldsymbol{b}_i\right)\beta_i-\boldsymbol{T}\right\|. \tag{8}$$

Under normal circumstances, the number of hidden nodes is much smaller than that of input nodes, so $\boldsymbol{H}$ is usually singular, and the expected output weight matrix can be calculated as

$$\hat{\boldsymbol{\beta}}=\boldsymbol{H}^{+}\boldsymbol{T}, \tag{9}$$

where $\boldsymbol{H}^{+}$ is the Moore-Penrose generalized inverse matrix of $\boldsymbol{H}$.

As has been mentioned, the input weight and threshold matrix of ELM are randomly generated, so it still causes a certain size of prediction error. To improve the prediction accuracy of the neural network, the PSO algorithm is used to optimize the ELM by finding the optimal values of these two parameters, so that the optimal output weight matrix can be obtained through ELM training. This combined algorithm is defined as the PSO-ELM algorithm, whose specific process is shown in Fig.2.

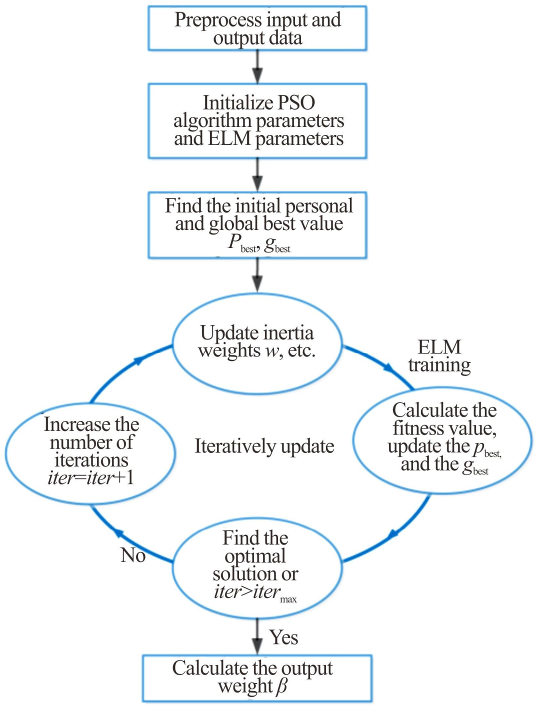

Fig.2 Flow chart of PSO-ELM algorithm

The PSO-ELM algorithm steps are as follows.

1. Data pre-processing. The experimental data are divided into training and predicted datasets and normalized.

2. Set the initial variables of the ELM neural network and the relevant initial parameters of the PSO algorithm, such as the learning factor c_1 and c_2, inertia weight w, the maximum number of iterations $iter_{\max}$, etc. The ith particle can be expressed as $\boldsymbol{X}_i=[W_{11}, \ldots,W_{L1},\ldots,W_{1n},\ldots,W_{Ln}, \boldsymbol{b}_1,\ldots,\boldsymbol{b}_L]$, where W_{ij} (j=1,…,L; i=1,…,n) is the input weight between the ith input node and the jth hidden node, and $\boldsymbol{b}_j$ is the threshold value of the jth hidden node.

3. Find the initial extremum. Substitute the training data into the ELM neural network for training based on the initial position of the particles, and calculate the ELM output value. In terms of the fitness value, find individual and group extreme values, and record their values and locations. The fitness function is selected as

$$\frac{1}{N}\sum_{i=1}^{n}(Y_i-\hat{Y}_i)^2. \tag{10}$$

4. Update the inertia weight. The inertia weight should decrease linearly with the number of iterations for the sake of global search ability in the early stage and local search ability in the later stage. Thus, we can make the inertia weight of each iteration w_{iter} decrease linearly by reference to

$$w_{\mathrm{iter}}=w_{\max}\cdot\left(w_{\max}-{}^{w_{\min}}\!/_{w_{\min}}\right)\cdot iter, \tag{11}$$

where $w_{\max}$ and $w_{\min}$ are the maximum and the minimum inertia weights, respectively, and $iter$ is the number of iterations.

5. Iterative optimization. In each iteration process,

every particle updates its speed and position according to the individual extreme value and the group extreme value, and finally gets the best individual fitness value and position.

6. Calculate the output weight of the ELM model. The final optimal position of the individual represents the optimal input weight matrix and threshold matrix that we need, which can be substituted into the ELM neural network to obtain the optimal output weight β.

The experiment object to be tested was an aluminum alloy plate forming the structure of the spacecraft cabin, which was 660 mm in length, 660 mm in width, and 3 mm in thickness. The frame around the plate was fixed and will not be deformed during the experiment. The length of the fixed part was 30 mm and 33 mm respectively. The experimental system diagram is given in Fig.3(a), as well as the working principle in Fig.3(b). The experimental system was composed of a quasi-distributed FBG sensor network, a dial indicator array, a demodulator, two remote-controlled motors, and a computer. The performance parameters of the experimental system are set as listed in Tab.1.

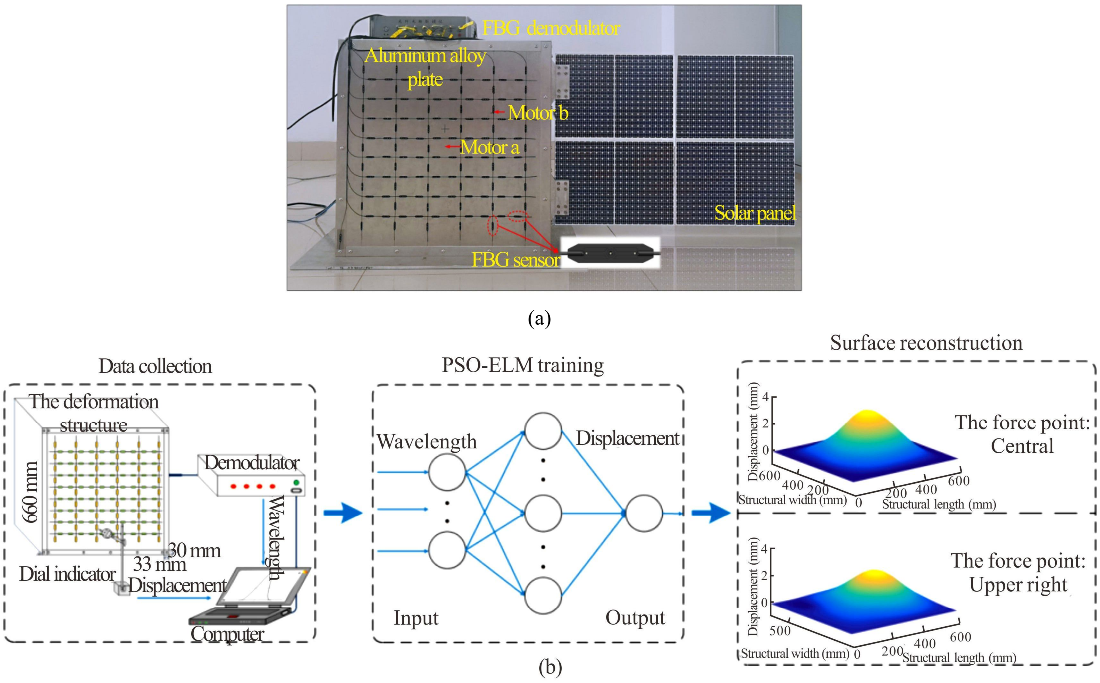

Fig.3 (a) Experimental system diagram; (b) Experimental system model and work principle

Tab.1 Technical data used for the experimental system

Parameter	Value
Number of sensors	134
Wavelength coverage	1 532—1 554 nm
Sensor sensitivity	1.22 pm/με
Sampling frequency	100 Hz
Accuracy of displacement measuring	0.001 mm

The FBG sensor and dial indicator measuring points were reasonably arranged based on space division multiplexing technology, wavelength division multiplexing technology, and characteristics of the tested structure. The layout of the FBG sensors and dial indicators is shown in Fig.4. As we can see, there were 14 channels in the sensor network, namely, 8 horizontal channels and 6 vertical channels. Each horizontal channel contained 10 sensors, and each longitudinal channel contained 9 sensors, to realize the collection of strain data of 134 measuring points in both horizontal and vertical directions of the deformable part of the entire plate. At the same time, 20 dial indicator measuring points were arranged to measure the real deformed displacement of the structure. The indicator measuring points were represented by red dots as shown in Fig.4.

In the system, two motors were installed to provide load force to cause structural deformation. One motor was placed in the center area of the plate (herein referred to Motor a), and the coordinate position in Fig.4 is (330 mm, 330 mm). Another one was placed in the upper right corner area of the plate (herein referred to Motor b), whose coordinate position is (480 mm, 440 mm), as shown by red and blue crosses respectively in Fig.4. Control the action of motors in different areas to occur different types of deformation of the plate structure, thereby different kinds of data correspondingly will be generated for the experiment.

The whole experiment works as follows. The aluminum alloy plate is deformed induced by the load force of the installed motors, which will cause a shift of the Bragg wavelength of the FBG sensors. The wavelength information is demodulated by the demodulator and transferred to the computer, as well as the displacement information measured by the dial indicators to be displayed and stored. Afterwards, these two kinds of the dataset are processed by the PSO-ELM algorithm to obtain a predicted model, for the reconstruction of the tested structure.

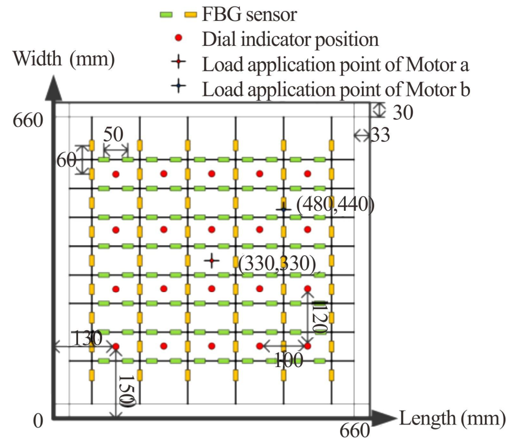

Fig.4 Layout diagram of the device

The two motors placed in this experiment can apply three kinds of thrusts that increase sequentially in steps according to the distance of applied force in steps. The stepping amount of the motor is shown in Tab.2.

Tab.2 Step amount of motors

Motor number	Step 1 (mm)	Step 2 (mm)	Step 3 (mm)
Motor a	1.383	2.554	3.709
Motor b	0.530	1.504	2.147

Therefore, these two motors apply different load forces at different positions, so that 12 deformation states of the structure can be obtained. In this experiment, a total of 120 sets of data were collected for neural network training and prediction that meet the requirements.

The data collected as the motors applied the load force of step 2 and step 3 was used as the training dataset, and the rest data collected as the motors applied the load force of step 1 was used as the predicted dataset. To reduce the experimental serendipity, the data sequence was disrupted before training. Both in the training dataset and the prediction dataset, the wavelength data gauged by FBG sensors was regarded as the input, the corresponding displacement data measured by dial indicators was regarded as the output, and they were introduced into the PSO-ELM algorithm for training and predicting to obtain a predicted model. The number of hidden nodes has a great impact on the training performance of the neural network. The larger the number of nodes, the higher the training accuracy, but the run-time will increase correspondingly. Therefore, in this experiment, as the prerequisite of the total number of particle swarms in the PSO algorithm was set to 30, make the number of hidden nodes in the ELM network change to determine the optimal one by observing the change in fitness function values, run-time and training errors. To further reduce the serendipity of the experiment, each case of the number of hidden nodes will be run 10 times, and the average value of each parameter will be taken for subsequent analysis.

Throughout the ELM theory, when the number of training data is equal to the number of hidden nodes, the output matrix of the hidden layer will change to be invertible, which means that the predicted value could be exactly the same as the actual value, leading to zero error in fitting theoretically. Thus, it is not meaningful to increase the number of nodes continuously. However, in practice, if the number of training data is large enough to make overfitting occur early before the number of hidden nodes gets close to the number of training data, it will cause the model to lose its fitting ability in an early stage. According to Fig.5 and Fig.6, considering the run-time, fitness value together with the training errors, the number of hidden nodes was tuned to 7, and the particle swarm size parameter in the PSO algorithm was tuned to 30.

In the PSO algorithm, the fitness function is selected as Eq.(10).

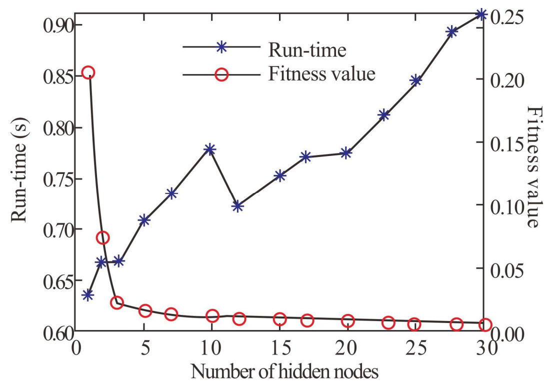

Fig.5 Run-time and fitness value as a function of the number of hidden nodes

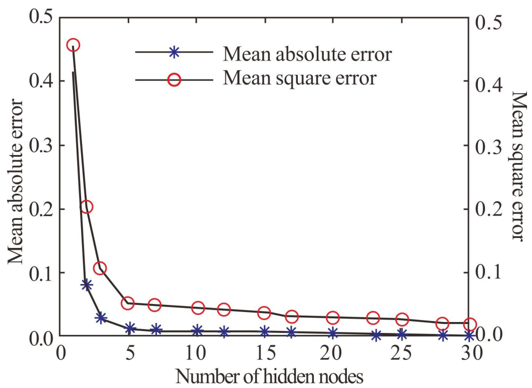

Fig.6 Mean absolute error and mean square error as a function of the number of hidden nodes

As shown in Fig.7, the fitness value decreases and the training accuracy improves with the increase of the number of iterations. It means that the optimal input weight and threshold matrix are approached as the iteration progresses by the PSO algorithm.

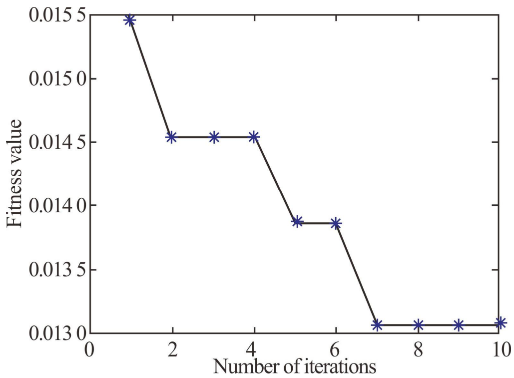

Fig.7 Fitness value as a function of the number of iterations

Comparing the prediction results of the PSO-ELM predicted model with the standard ELM predicted model and the traditional curvature conversion method (CCM), the errors of these three methods are shown in Tab.3. It can be seen that the PSO-ELM predicted model comes to a higher time cost, whose run-time has increased from 0.13 s to 0.73 s. Compared with the standard ELM predicted model, its reconstruction accuracy is greatly improved, significantly higher than that of the standard ELM model and curvature conversion method, with the mean absolute error of 0.50 mm and mean square error of 0.009. Therefore, the advantages of the algorithm proposed for structural deformation displacement field reconstruction are further verified.

Tab.3 Reconstruction errors for PSO-ELM, ELM and CCM

Algorithm	Run-time (s)	Mean absolute error (mm)	Mean square error
PSO-ELM	0.73	0.050	0.009
ELM	0.13	0.267	0.169
CCM	/	0.422	0.271

One main reason for the increasing time is that in the PSO-ELM algorithm, the extra time must be paid to find the optimal input weight and hidden layer threshold matrix in a loop to obtain the optimal output weight matrix. However, in the standard ELM predicted model, once the input weight and hidden layer threshold matrix are randomly generated, they no longer change. Therefore, the run-time of the PSO-ELM is much longer than that of the standard ELM. As a whole, on the premise of meeting the detection requirements, it is worthwhile to sacrifice the run-time factor to achieve an improvement of numerical accuracy.

Fig.8 shows the predicted and measured values of a set of data for the ELM and PSO-ELM predicted models. It can be demonstrated that the predicted values do not fit well with the measured values, and even many points have large errors in the way of the ELM algorithm. In contrast, when training by the PSO-ELM algorithm, the predicted values and measured values basically overlap, and only a few predicted points deviate from the actual points. Thus, it can be concluded that the PSO-ELM algorithm presents significantly better performance than the ELM algorithm, and makes great progress in the enhancement of the deformed accuracy.

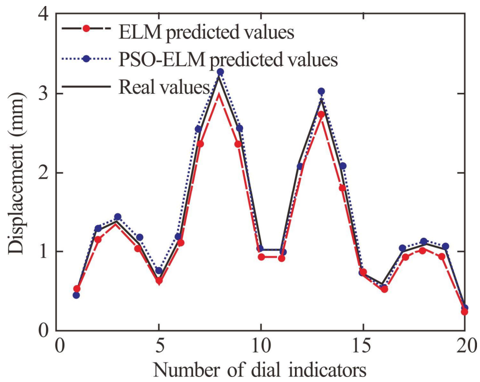

Fig.8 Comparison of the real and predicted values for PSO-ELM predicted model and ELM predicted model

Using the measured displacement data collected by testing and the predicted data by the PSO-ELM predicted model to reconstruct the surface with the cubic spline interpolation method, the results are shown in Fig.9. The error surface is drawn by the difference between the real measured data and the predicted data, whose root mean square error is less than 0.003 5, which proves that the surface fitted by the predicted displacement and the actual surface are substantially coincident to meet the surface reconstruction requirements.

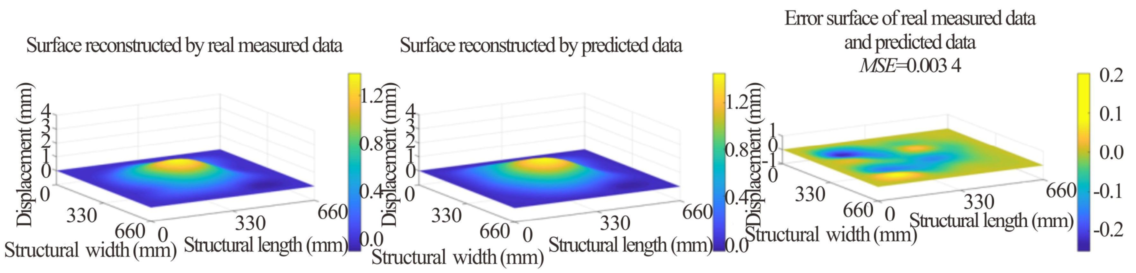

(a)

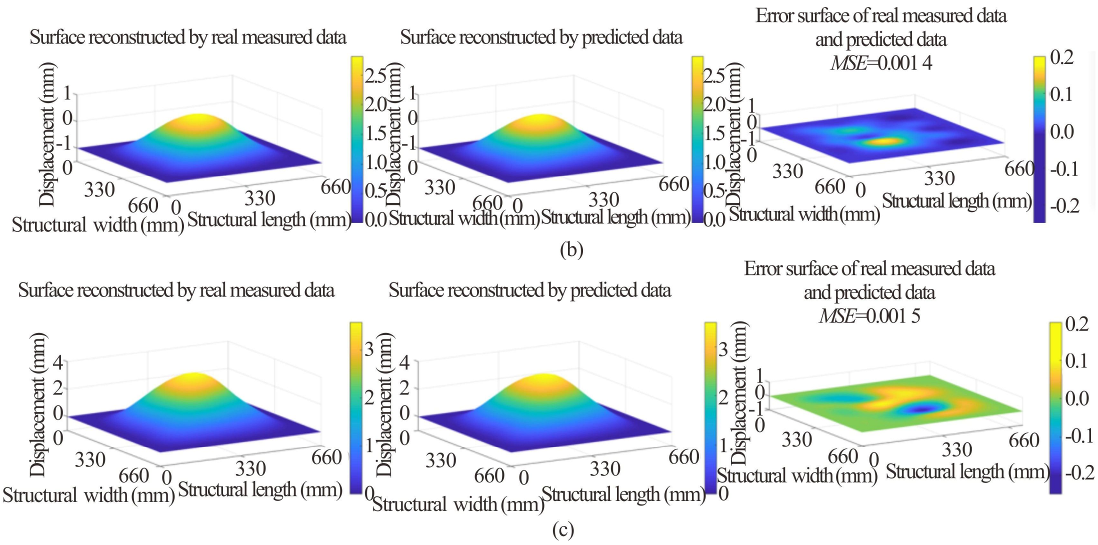

Fig.9 Comparison of the reconstructed surfaces using measured value and predicted value, respectively in different load cases: (a) Motor a with load force of step 1, while Motor b without load force; (b) Motor a with the maximum load force, and Motor b with load force of step 2; (c) Both Motor a and Motor b with the maximum load force

The motors were used to apply different steps of load force to the tested structure, so that it can get different types of deformation. After the feasibility of the PSO-ELM model has been verified, the deformation process of the aluminum alloy plate could be reconstructed validly by substituting the data collected under different steps used as the predicted dataset sequentially and the rest of the data used as the training dataset into the PSO-ELM predicted model for training, prediction, and then the obtained discrete data was reconstructed by the same way for surface reconstruction, which is shown in Fig.10. It suggests that the combination of FBG sensor array and ELM optimized by PSO algorithm can accurately realize the visual reconstruction of aluminum alloy plate under different deformation states.

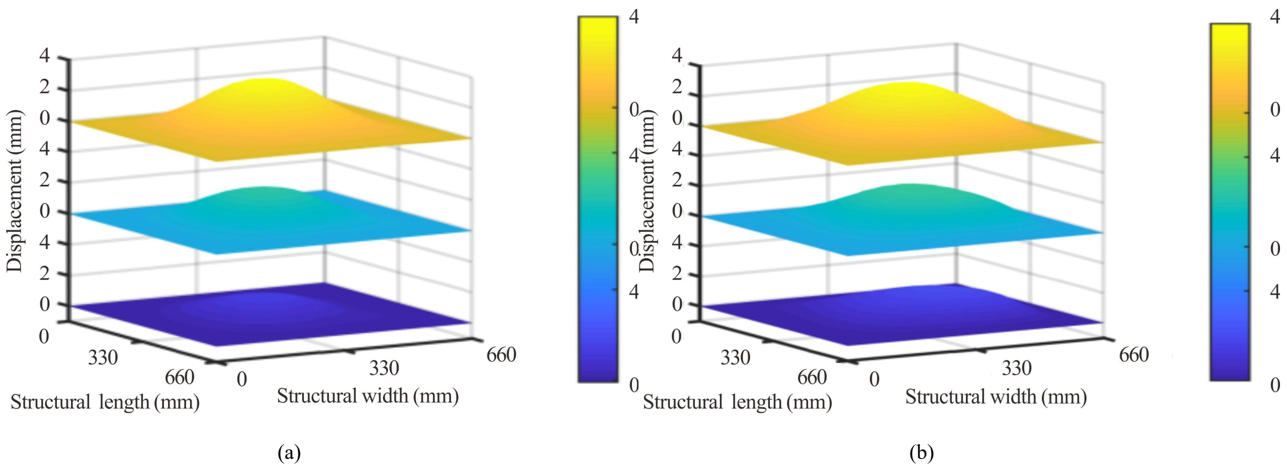

Fig.10 Reconstruction of deformation process of the structure in different load cases: (a) Motor b without load force, while Motor a with load force from step 1 to step 3; (b) Motor b with the maximum load force, while Motor a with load force from step 1 to step 3

This paper proposes a visual reconstruction method of the flexible structure based on the FBG sensor array and the ELM optimized by the PSO algorithm, which realizes the visual reconstruction of an aluminum alloy plate under different deformation states. Compared with the traditional surface reconstruction methods, the proposed method has lower requirements for the deformed structure, and the surface reconstruction can be realized without considering the structural material information in the experiment. Since the input dataset for training is too large, resulting in a slower learning speed and longer run-time for the PSO-ELM network than the standard ELM network, the neural network will be further optimized in subsequent studies by reducing the run-time.

Statements and Declarations

The authors declare that there are no conflicts of interest related to this article.

References

[1] GE J, JAMES A E, XU L, et al. Bidirectional soft silicone curvature sensor based on off-centered embedded fiber Bragg grating[J]. IEEE photonics technology letters, 2016, 28(20)：2237-2240.

[2] SUN G, LI H, DONG M, et al. Optical fiber shape sensing of polyimide skin for a flexible morphing wing[J]. Applied optics, 2017, 56(33)：9325-9332.

[3] TATABE K, ISHIKAWA K, OIKAWA Y. Compensation of fringe distortion for phase-shifting three-dimensional shape measurement by inverse map estimation[J]. Applied optics, 2016, 55(22)：6017-6024.

[4] WEI Y, GAO F. Architecture design method for structural health monitoring system (SHM) of civil aircraft[C]//International Conference on Sensing, Diagnostics, Prognostics, and Control, August 16-18, 2017, Shanghai, China. New York：IEEE, 2017：736-739.

[5] BANG H J, JANG M, SHIN H, et al. Structural health monitoring of wind turbines using fiber Bragg grating based sensing system[J]. Proc. SPIE, 2011, 7981：79812H-79812H-8.

[6] SAHOTA J K, GUPTA N, DHAWAN D. Fiber Bragg grating sensors for monitoring of physical parameters：a comprehensive review[J]. Optical engineering, 2020, 59(6)：1.

[7] ZENG J, WANG W, WANG B, et al. Sensitivity of optical FBG sensor under dynamic/static load[J]. Journal of Nanjing University of Aeronautics & Astronautics, 2015, 47(03)：397-402. (in Chinese)

[8] ZHU X, LU M, FAN H, et al. Experimental research on intelligent structure vibration shape perception and reconstruction based on fiber grating network[J]. Chinese journal of scientific instrument, 2009, 30(001)：65-70. (in Chinese)

[9] ZHANG H, ZHU X, LI L, et al. Space curved surface reconstruction method using two-dimensional curvature data[J]. Journal of basic science and engineering, 2015, 23(05)：1035-1046. (in Chinese)

[10] WANG C. 3D shapes detecting method of soft manipulator based on fiber Bragg grating sensor[J]. Control and instruments in chemical industry, 2015, 42(010)：1130-1133. (in Chinese)

[11] ZHENG J, QIAN J, SHEN L, et al. Surface reconstruction of 3D curved surface based on information of spatial curvature[J]. Journal of Shanghai University, 2009, 15(03)：235-237, 250. (in Chinese)

[12] THOMAS J, GURUSAMY S, RAJANNA T R, et al. Structural shape estimation by mode shapes using fiber Bragg grating sensors：a genetic algorithm approach[J]. IEEE sensors journal, 2020, 20(6)：2945-2952.

[13] BANG H J, KO S W, JANG M S, et al. Shape estimation and health monitoring of wind turbine tower using a FBG sensor array[C]//2012 IEEE International Instrumentation and Measurement Technology Conference Proceedings, May 13-16, 2012, Graz, Austria. New York：IEEE, 2012：496-500.

[14] TESSLER A, SPANGLER J L. A least-squares variational method for full-field reconstruction of elastic deformations in shear-deformable plates and shells[J]. Computer methods in applied mechanics & engineering, 2005, 194(2-5)：327-339.

[15] MAO Z, TODD M. Comparison of shape reconstruction strategies in a complex flexible structure[J]. Proc. SPIE, 2008, 6932：69320H-69320H-12.

[16] MISHRA M, SRIVASTAVA M. A view of artificial neural network[C]//2014 International Conference on Advances in Engineering & Technology Research (ICAETR-2014), August 1-2, 2014, Unnao, India. New York：IEEE, 2014：1-3.

[17] HUANG G B, ZHU Q Y, SIEW C K. Extreme learning machine：a new learning scheme of feedforward neural networks[C]//2004 IEEE International Joint Conference on Neural Networks (IEEE Cat. No.04CH37541), July 25-29, 2004, Budapest, Hungary. New York：IEEE, 2004：985-990.

[18] WANG Y, CAO F, YUAN Y. A study on effectiveness of extreme learning machine[J]. Neurocomputing, 2011, 74(16)：2483-2490.

[19] DING S, XU X, NIE R. Extreme learning machine and its applications[J]. Neural computing and applications, 2013, 25(3-4)：549-556.

[20] WAN C, XU Z, PINSON P, et al. Optimal prediction intervals of wind power generation[J]. IEEE transactions on power systems, 2014, 29(3)：1166-1174.

[21] YE T, JIAN M, CHEN L, et al. Rolling bearing fault diagnosis under variable conditions using LMD-SVD and extreme learning machine[J]. Mechanism and machine theory, 2015, 90：175-186.

[22] KENNEDY J, EBERHART R. Particle swarm optimization[C]//Proceedings of ICNN'95 - International Conference on Neural Networks, November 27 - December 1, 1995, Perth, WA, Australia. New York：IEEE, 1995：1942-1948.

[23] TRELEA I C. The particle swarm optimization algorithm：convergence analysis and parameter selection[J]. Information processing letters, 2003, 85(6)：317-325.

[24] WANG D, MENG L. Performance analysis and parameter selection of PSO algorithms[J]. Acta automatica sinica, 2016, 42(010)：1552-1561. (in Chinese)

[25] KINET D, MÉGRET P, GOOSSEN K W, et al. Fiber Bragg grating sensors toward structural health monitoring in composite materials：challenges and solutions[J]. Sensors (Basel, Switzerland), 2014, 14(4)：7394-7419.

[26] HILL K O, MELTZ G. Fiber Bragg grating technology fundamentals and overview[J]. Journal of lightwave technology, 1997, 15(8)：1263-1276.

[27] ALVAREZ-BOTERO G, BARON F E, CANO C C, et al. Optical sensing using fiber Bragg gratings：fundamentals and applications[J]. IEEE instrumentation & measurement magazine, 2017, 20(2)：33-38.

[28] ZHANG S, CHEN M, HE Q, et al. Quasidistributed fiber Bragg grating sensor network based on self-heterodyne detection technique[J]. Optical engineering, 2014, 53(5)：057107.